AIP Advances

RESEARCH ARTICLE | AUGUST 06 2026

Dynamic response of a magnetizable single fiber in an AC magnetic field for contactless particle detachment in gas-phase filtration

Nadine May ; Jörg Meyer ; Matthias Franzreb ; Achim Dittler

Check for updates

AIP Advances 16, 085013 (2026)
https://doi.org/10.1063/5.0336631

View Online
Export Citation

Articles You May Be Interested In

Locomotion through soft materials of paired solid spheres as a miniature robot

AIP Advances (February 2023)

An insulator-based dielectrophoretic microdevice for the simultaneous filtration and focusing of biological cells

Biomicrofluidics (October 2011)

Local mapping of interface traps using contactless capacitance transient technique

AIP Advances (October 2016)

10 August 2026 14:38:49

AIP Publishing

Special Topics Open for Submissions

Learn More

AIP Publishing

Dynamic response of a magnetizable single fiber in an AC magnetic field for contactless particle detachment in gas-phase filtration

Cite as: AIP Advances 16, 085013 (2026); doi: 10.1063/5.0336631
Submitted: 13 April 2026 • Accepted: 19 July 2026 •
Published Online: 6 August 2026

View Online Export Citation CrossMark

Nadine May,[1,a)] Jörg Meyer,[1] Matthias Franzreb,[2] and Achim Dittler[1]

AFFILIATIONS

[1] Karlsruhe Institute of Technology, Institute of Mechanical Process Engineering and Mechanics, Straße am Forum 8, 76131 Karlsruhe, Germany

[2] Karlsruhe Institute of Technology, Institute of Functional Interfaces, Hermann-von-Helmholtz-Platz 1, 76344 Eggenstein-Leopoldshafen, Germany

[a)] **Author to whom correspondence should be addressed:** nadine.may@kit.edu

10 August 2026 14:38:49

ABSTRACT

The dynamic behavior of a magnetizable single fiber exposed to a spatially homogeneous alternating magnetic field was investigated experimentally and numerically with the purpose of laying the foundations for subsequent contactless particle removal in gas-phase filtration. A Helmholtz coil arrangement was used to generate a well-defined AC magnetic field, which was characterized by Hall probe measurements and finite element simulations using COMSOL Multiphysics®. A ferritic stainless steel fiber clamped at one end was excited by the aligning magnetic torque induced by the alternating magnetic field with sinusoidal time dependence. High-speed imaging combined with automated MATLAB-based motion analysis enabled the determination of deflection, velocity, and acceleration. The steady-state response exhibits harmonic oscillation at the driving frequency (35–55 Hz) and can be accurately described by the analytical solution of a driven damped harmonic oscillator. A pronounced resonance peak was observed near the theoretically predicted natural frequency ($f_{0,\text{theo.}}$ = 49.2 Hz). The transient response reveals a superposition of the natural and driving frequencies, leading to beat phenomena for off-resonant excitation. The experimentally determined frequency response agrees well with the analytical model and confirms the interpretation of the distributed magnetic torque as an effective modal driving force. The results provide a consistent physical framework for magnetically induced oscillations of slender structures and form the basis for future studies on particle detachment from particle-laden magnetizable fibers.

© 2026 Author(s). All article content, except where otherwise noted, is licensed under a Creative Commons Attribution (CC BY) license (https://creativecommons.org/licenses/by/4.0/). https://doi.org/10.1063/5.0336631

I. INTRODUCTION

In many chemical and process engineering applications, filters are employed to remove particulate matter from gas streams. These filters are often surface-type filters that accumulate layers of particles over time and consequently require periodic cleaning to maintain performance in terms of permeability. Depending on the specific process, cleaning is typically achieved either by applying a reverse-pressure pulse,[1] backflushing, or mechanical shaking. In several gas-phase processes, however, conventional cleaning strategies are either technically infeasible or undesirable. This applies, for example, to compact or miniaturized filtration systems, where pressure pulses would disrupt the entire flow field; to high-temperature processes, where mechanical actuation is limited by material constraints; and to systems handling toxic, explosive, or highly reactive gases, where additional valves and moving parts increase safety risks. Furthermore, in strictly continuous processes, transient flow reversal may interfere with reaction kinetics or product quality. In such cases, a contactless actuation principle that does not require flow interruption or internal mechanical components is highly attractive.

To address this limitation, a novel approach is being explored in which cleaning is achieved through magnetically induced motion. In this concept, a single magnetizable steel fiber is excited by an alternating magnetic field, causing it to oscillate in a controlled manner. In future studies, the resulting fiber oscillations are expected to facilitate the detachment of particle structures from its surface.

A Helmholtz configuration is particularly advantageous for fundamental investigations, as it provides a spatially homogeneous and mathematically well-defined magnetic field, enabling precise comparisons among experiments, analytical theory, and numerical simulations. When a magnetizable fiber clamped at one end is placed within a spatially homogeneous magnetic field, no net translational magnetic force arises due to the absence of field gradients. Instead, the interaction between the induced magnetic moment of the fiber and the external magnetic field generates an aligning magnetic torque.[2] This torque tends to orient the effective magnetic moment of the fiber parallel to the applied field.

Under sinusoidal excitation, the time-dependent magnetic field produces a correspondingly time-varying torque that acts as a distributed rotational excitation along the fiber axis. This torque induces bending motion as the elastic restoring forces of the slender structure oppose the magnetic alignment. The resulting dynamics are governed by the interplay among magnetic torque, elastic stiffness, inertia, and damping. Consequently, the fiber behaves as a torque-driven damped oscillator.

In the present work, we experimentally and numerically investigate the oscillation behavior of a single magnetizable fiber subjected to a sinusoidal magnetic field generated by Helmholtz coils. The magnetic field is characterized both experimentally and by finite element simulations using COMSOL Multiphysics®, ensuring a quantitative description of the field amplitude and spatial distribution under alternating current excitation. The fiber motion is recorded using high-speed imaging, and the time-resolved deflection is evaluated by automated image processing in MATLAB®, enabling the determination of deflection, velocity, and acceleration.

Particular attention is paid to the temporal evolution of the fiber response. Upon activation of the alternating magnetic field, the system exhibits a transient response characterized by the superposition of two oscillatory components: the intrinsic resonance frequency of the fiber and the externally imposed driving frequency. As the system evolves in time, the resonance component is progressively damped, and the motion converges toward a steady-state response dominated solely by the driving frequency. This behavior reflects the classical response of a driven damped oscillator; yet, in the present case, the forcing mechanism arises from distributed magnetic interactions rather than mechanical base excitation or point loading. Beyond the fundamental interest in magneto-mechanical coupling, the investigated configuration provides a physical basis for future applications in particle-laden fiber systems. Magnetically induced oscillations may offer a contactless strategy for detaching deposited particulate structures in situations where conventional cleaning methods, such as flow reversal or mechanical agitation, are not feasible.

II. MATERIALS AND METHODS

The experimental setup essentially consists of Helmholtz coils supplied with an AC source, a magnetizable fiber clamped on one side to a fiber holder, and a high-speed camera that records the fiber movement. The overall experimental setup is shown in Fig. 1 and will be described in more detail in the following sections.

A. Helmholtz coils

Two vertically installed Helmholtz coils are used to generate a spatially homogeneous alternating field in the central free space of the coil arrangement. The exact geometric data can be found in Fig. 2. The winding is wrapped around a PEEK coil form, and the two coils are connected in series so that the same current is guaranteed in both coils.

The coils each have 803 turns, using coated copper wire with a diameter of 0.8 mm. The polyurethane coating serves as electrical insulation, preventing short circuits between adjacent windings. The DC resistance of the coils, measured using a multimeter, is 9.34 and 9.26 Ω in coil Nos. 1 and 2, respectively. The complex resistance was determined using impedance spectroscopy, and the absolute value of the impedance Z is shown as a function of the frequency in Fig. 3.

As a derived value from impedance spectroscopy, the inductances of the coils are $L_1 = 76.17$ mH and $L_2 = 75.45$ mH, respectively. The inductance was also calculated on the basis of the coil parameters using empirical formulas[3] and results in $L_{theor.} = 74.98$ mH. Since the coils are inductively coupled, the opposing coil must be taken into account in a Helmholtz arrangement,[4] and the total inductance of the coil assembly is 185 mH (calculated).

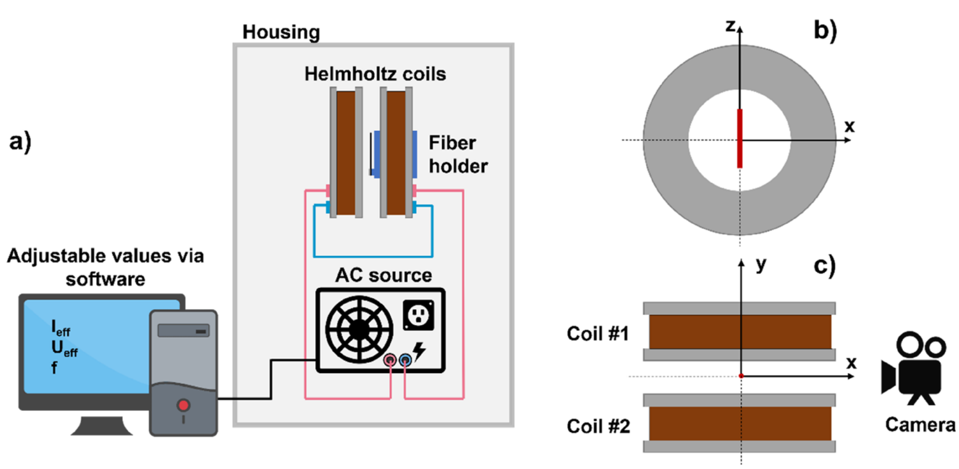

FIG. 1. (a) Front view of the experimental setup with vertically installed Helmholtz coils and fiber holder. (b) Side view of the Helmholtz coils with fixed coordinate system (fiber position marked in red). (c) Top view of the Helmholtz coils with viewing angle of the high-speed camera.

10 August 2026 14:38:49

© Author(s) 2026

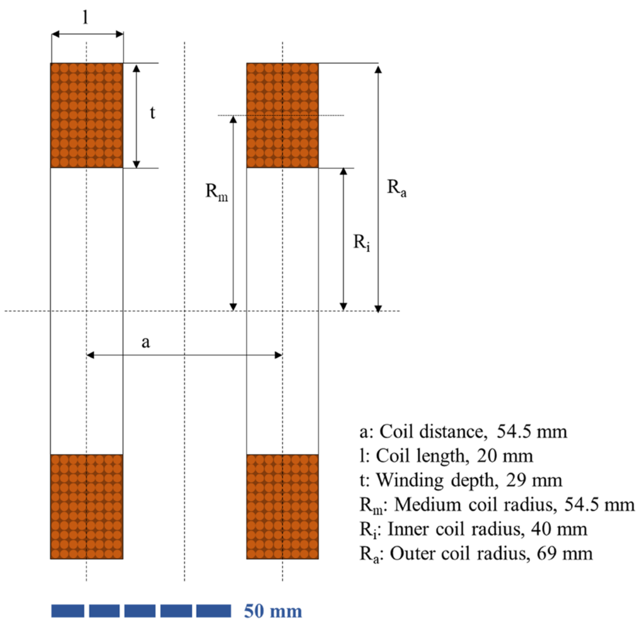

FIG. 2. Cross-sectional view of the Helmholtz coils with relevant dimensions.

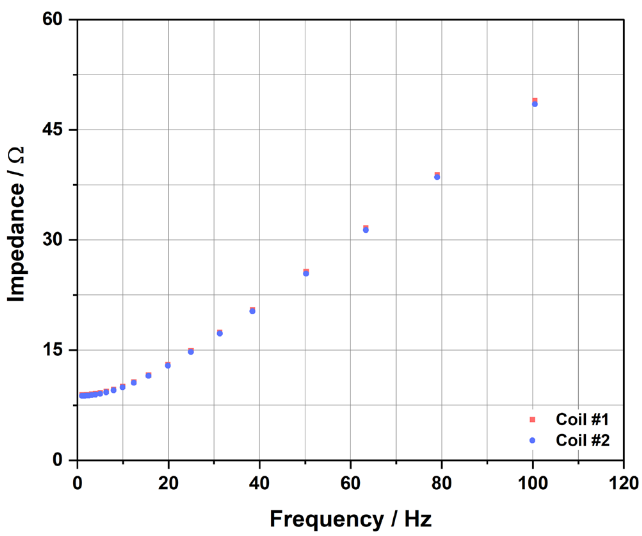

FIG. 3. Absolute value of the impedance Z over frequency for both coils.

The total inductance of the coils is decisive for how quickly the coils react to the flowing current and how quickly the resulting magnetic field can build up.

The coils are driven by an AC power source (AVF-P-1250, Preen AC Power Corp., Taipei, Taiwan). The output voltage and frequency are set via dedicated control software before enabling the signal output. The output trigger signal of the power source is additionally used to synchronize the high-speed camera, allowing precise recording of the transient fiber response immediately after field activation. The effective values of current and voltage are monitored directly within the control software. In the homogeneous magnetic field of the Helmholtz coils, the magnetic flux in this case is predominantly oriented along the y-direction, such that the magnetic flux density vector B is mainly composed of a y-component (B_y), which is measured using a Hall probe (FH51, Dr. Steingroever GmbH, Cologne, Germany). The probe detects only those components of the magnetic field that are perpendicular to the sensor surface. Depending on the sensor orientation, either an axial or a transversal probe is employed to measure B_y. The instrument supports both DC and AC measurement modes; in AC mode, the effective (RMS) magnetic flux density is recorded.

B. Fiber properties and recording of fiber movement

The fiber material used in this study is ferritic stainless steel (EN 1.4016, AISI 430) with a diameter of 95 μm and a free length of 3.8 cm.

From the fiber geometry and the material properties, which are summarized in Table I, the natural frequency f_0 can be calculated using the following equation, assuming that the arrangement corresponds to an Euler–Bernoulli beam clamped on one side:[5]

$$f_0 = \frac{1.875^2}{2\pi}\sqrt{\frac{EI}{\rho A l_F^4}}, \tag{1}$$

where I is the surface moment of inertia, $I = \frac{\pi}{64}d_F^4$, and A is the cross-sectional area, $A = \frac{\pi}{4}d_F^2$.

The resulting first natural frequencies are shown below as a function of the fiber length [see Fig. 4(a)] and the fiber diameter [see Fig. 4(b)]. The dimensions used for diameter and length are marked in red.

The used fiber geometry has a calculated natural frequency of 49.20 Hz.

The fiber is clamped on one side in a PEEK fiber holder and pushed into coil No. 1. The resulting geometry and the corresponding defined coordinate system can be seen in Fig. 1. The fiber is located in the center plane between the coils and is oriented vertically.

The fiber oscillation is recorded using a high-speed camera (Q-VIT, AOS Technologies AG, Baden Dättwil, Switzerland) that must be externally triggered. To capture the onset of the oscillation (transient response), the output signal of the AC source can be used as a trigger for the camera. In contrast, to record the steady oscillation (steady-state response), which occurs a few seconds after the alternating magnetic field is switched on, the camera can also be triggered manually.

TABLE I. Specification of the used fibers.

Material	Ferritic steel, 1.4016 (X6Cr17)
Young's modulus E (GPa)	220
Bulk density ρ (kg m^3)	7700
Diameter d_F (μm)	95
Length l_F (cm)	3.8
Mass m_F (mg)	2.074

10 August 2026 14:38:49

© Author(s) 2026

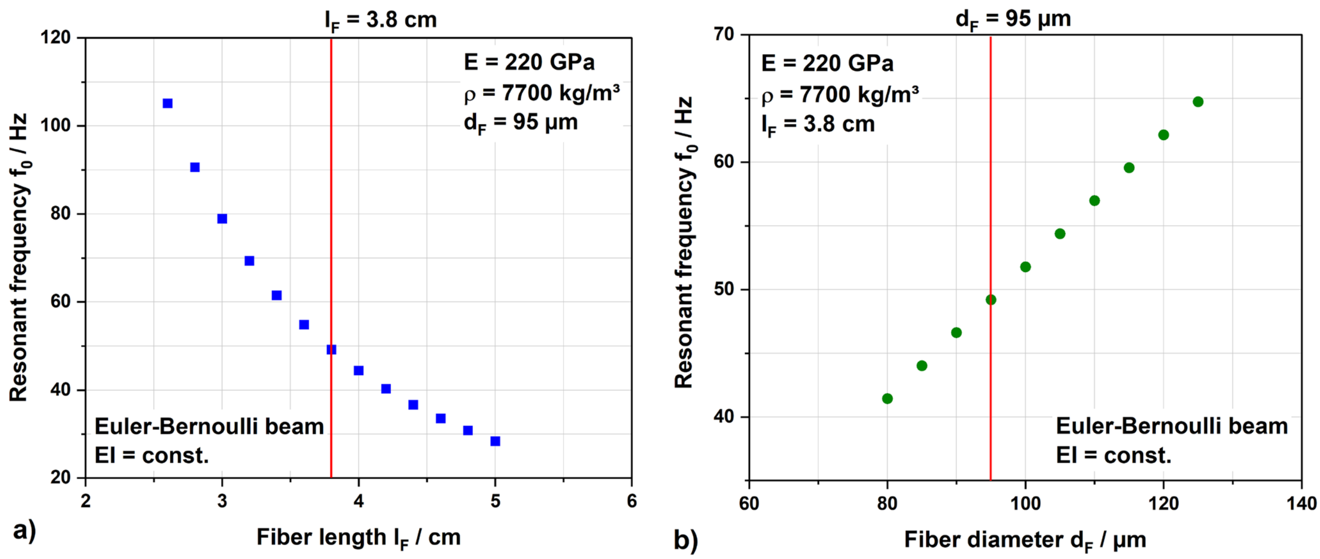

FIG. 4. Calculated natural frequency of a fiber clamped on one side as a function of (a) fiber length and (b) fiber diameter.

The camera is positioned on the *x*-axis at a distance of ~30 cm from the fiber. The oscillation of the fiber can thus be viewed in the *yz*-plane. The camera is equipped with a lens (Zoom 6000 Series, Navitar, Rochester, United States of America) that allows 6× magnification.

The recordings are all made at a frame rate of 1000 fps, whereby between 0.5 and 2 s are recorded in real time, which corresponds to 500–2000 frames. The shutter is set to an opening time of 350 µs and the resolution to 1280 × 1080 pixels in a corresponding field of view of 19 × 16 mm. At the end of each test series, a scale is recorded with the camera so that pixels can be converted into absolute dimensions during subsequent image evaluation.

C. MATLAB® evaluation of fiber movement

The recordings are then evaluated using a self-written MATLAB script.[6] The MATLAB script performs a video-based motion analysis of an oscillating fiber to determine its deflection, frequency, velocity, acceleration, and angular deflection. All processed data and experimental parameters are exported to an Excel file for documentation and further evaluation. The script extracts the frame rate, total number of processed frames, and video duration. In addition, the original recording frame rate and total number of frames (from the acquisition system) are entered manually to enable correct temporal scaling. The user manually selects a tracking point on the fiber, as illustrated schematically in Fig. 5.

In principle, any position along the fiber can be evaluated to obtain the corresponding displacement and acceleration. Although the fiber tip (3.8 cm) exhibits the largest deflection, a point located at 3.5 cm was consistently selected because it represents the furthest position that could be reliably tracked under all investigated operating conditions. This position, therefore, provides a large oscillation amplitude while ensuring robust image tracking and consistent displacement determination for all measurements.

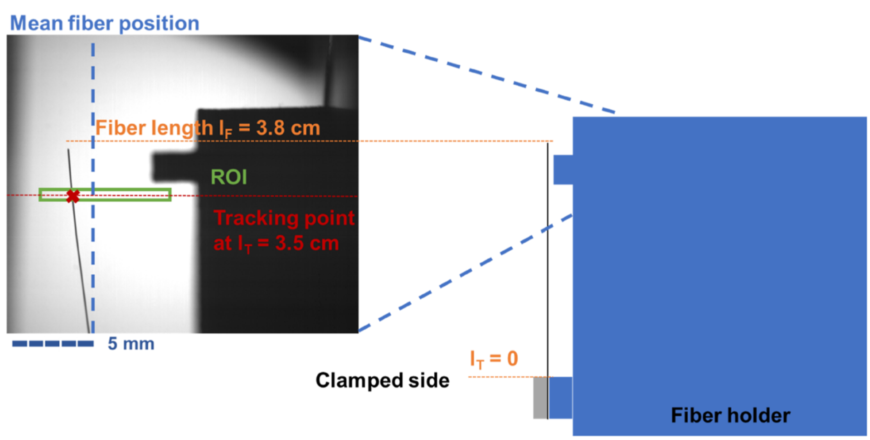

FIG. 5. Schematic representation for analysis using MATLAB script including tracking point (red), ROI (green), mean fiber position (blue), and fiber holder.

© Author(s) 2026
10 August 2026 14:38:49

The position of the tracking point is defined by the length l_T, where $l_T = 0$ corresponds to the clamped end of the fiber and $l_T = 3.8$ cm to the free end. A region of interest (ROI) around this point is defined interactively and can be adjusted iteratively based on a preview sequence. The ROI is chosen such that the fiber remains within this region even at its maximum oscillation amplitude. Within each frame, the tracking algorithm converts the frame to grayscale, enhances contrast, identifies the darkest pixel inside the ROI (assumed to correspond to the fiber), and stores its horizontal pixel coordinate. The coordinates can be converted to a physical scale (mm or cm) using a previously recorded calibration scale.

The post-processing of image-derived tracking data requires the computation of the second derivative of the fiber deflection to obtain the corresponding acceleration.

The displacement signal obtained from high-speed imaging contains small tracking fluctuations originating from image noise and sub-pixel detection uncertainty. Because numerical differentiation strongly amplifies high-frequency noise, especially when calculating the second derivative (acceleration), direct differentiation leads to nonphysical fluctuations in the acceleration signal.

To mitigate this effect, a Savitzky–Golay filter[7] was applied prior to differentiation, where the polynomial functions are derived instead of the measured values, whereby the calculated acceleration is also smoothed. While Savitzky–Golay filtering can theoretically attenuate high-frequency components and slightly reduce peak amplitudes if the filter window is chosen too large, this effect is negligible in the present study for two reasons. First, the fiber motion is dominated by a nearly monochromatic sinusoidal oscillation (in steady-state response) at the excitation frequency, meaning that no relevant physical high-frequency components are expected in the displacement signal. Second, the selected filter window (window length is set to 5) is significantly smaller than the oscillation period, ensuring preservation of the oscillation amplitude and phase while effectively suppressing measurement noise.

Therefore, the filtering primarily removes noise-induced artifacts without significantly affecting the peak acceleration or resonance behavior.

In addition, Savitzky–Golay filtering can introduce boundary effects because polynomial fitting near the signal edges is performed using asymmetric windows. These edge artifacts mainly affect a small number of samples at the beginning and end of the time series.

In this study, these boundary regions were excluded from quantitative analysis. Only the steady-state oscillation region, sufficiently far from the signal boundaries, was used for acceleration evaluation. Consequently, boundary effects do not influence the reported results.

D. COMSOL Multiphysics® simulation

The magnetic field generated by the Helmholtz coils was investigated experimentally and by numerical simulations using COMSOL Multiphysics (Version 6.3). The simulations were performed with the AC/DC Module employing the Magnetic Fields (mf) interface. The coil parameters described in Sec. II A were directly implemented in the numerical model.

Only the coils themselves were included in the simulation, while the coil body was omitted. The coil support is made of PEEK, which is a non-conductive and non-magnetic material and therefore does not influence the magnetic field. In contrast, coil bodies made of electrically conductive materials, such as aluminum, would need to be included in the model due to the formation of eddy currents that could modify the magnetic field distribution. To accurately represent the open magnetic field, the coil was embedded in a spherical air domain with a radius of 30 cm. The outermost 10 cm of this sphere were defined as an infinite-element domain, enabling a numerical approximation of an unbounded surrounding space while minimizing artificial boundary effects. Within the inner air domain, the magnetic field was solved using Ampère's Law. A magnetic insulation boundary condition was applied at the outer boundary of the infinite-element domain. This combination of a sufficiently large air domain, infinite elements, and magnetic insulation ensures that the computational boundaries do not influence the magnetic field distribution in the region of interest around the coil.

The simulated magnetic field reproduced the overall field distribution well; however, a systematic deviation of less than 5% between simulated and experimentally measured magnetic field values was observed. To achieve quantitative agreement between simulation and experiment, the model was calibrated by introducing an effective number of turns as an adjustable parameter. While the physical coils consist of 803 windings, an effective value of 825 turns was used in the simulation. With this adjustment, the simulated magnetic field matches the experimentally measured values within the experimental uncertainty. This effective parameter accounts for small geometric and experimental uncertainties that are not fully captured by the idealized coil model.[8]

III. RESULTS AND DISCUSSION

A. Magnetic field

The magnetic field was first measured at the center of the coil (position [x|y|z] = [0|0|0]), with the axial probe aligned so that the y-component of vector B, namely B_y, was recorded [compare Fig. 1(a)]. The effective current was varied for different frequencies. These measured points, including a linear fit over all frequencies, are shown in comparison with the calculation of the magnetic flux density according to Eq. (2) in Fig. 6.

The magnetic flux density at the center of the coil can be calculated using a simple formula:

$$B = \frac{8}{\sqrt{125}}\mu_0 \frac{NI}{a}, \tag{2}$$

where B is the magnetic flux density, N is the number of turns (here N = 803), I is the current, and a is the Helmholtz distance between the coils (here: a = 54.5 mm).

The magnetic flux density at the center of the Helmholtz coils exhibited an approximately linear dependence on the coil current for all investigated excitation frequencies (see Fig. 6), with only minor frequency-dependent differences. The fit, which is almost identical to the calculation, shows that the agreement is very good with an R^2 of 0.9986.

The measurement error, or deviation of the measured magnetic flux density from the calculation, can be seen in Fig. 7. Except for the first two points (at 50 and 100 mA), all points are within ±5%, which agrees with the specifications of the Hall sensor. The first measured

10 August 2026 14:38:49

© Author(s) 2026

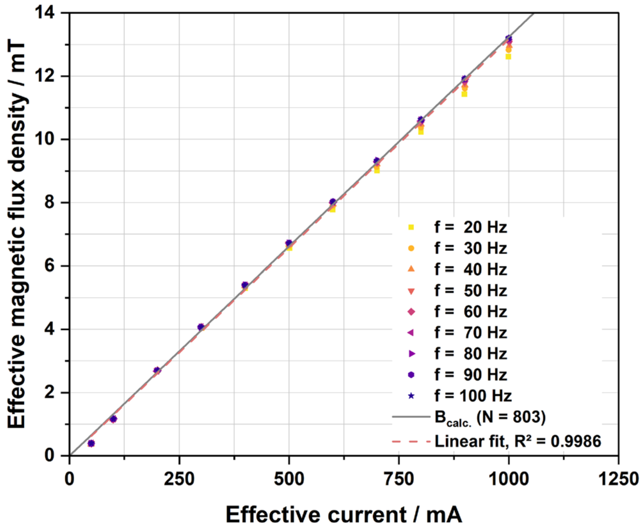

FIG. 6. Measured magnetic flux density at the center between the coils as a function of the effective current for different frequencies (symbols), and comparison with calculation results (black line) and a combined linear fit over all frequencies (red dashed line).

points at 50 and 100 mA are at the lower end of the measuring range of the sensor, which is why a larger error can occur here. At higher currents (750–1000 mA), the measurements obtained at lower frequencies deviate slightly more from the theoretical prediction. The observed deviations increase systematically at higher currents and lower frequencies; however, their exact origin cannot be conclusively identified. Since the magnetic field of an ideal Helmholtz coil is expected to scale linearly with current and to remain essentially frequency-independent over the investigated range, this behavior most likely originates from non-ideal experimental effects, such as the frequency response of the magnetic field sensor or measurement

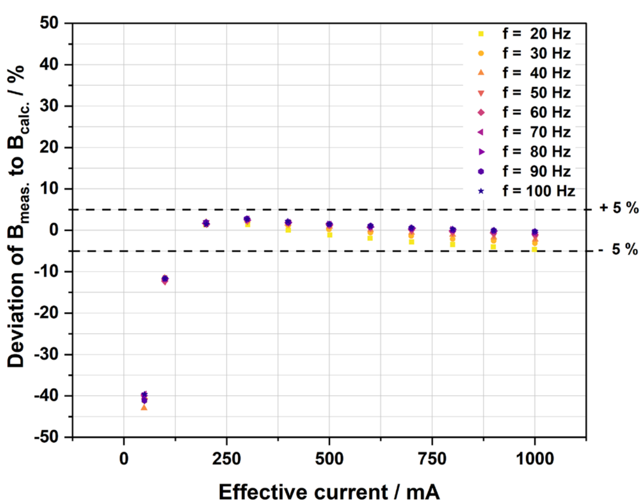

FIG. 7. Deviation between the measured and calculated magnetic flux density as a function of the effective current for different frequencies.

electronics, slight deviations of the actual coil current from the nominal value, and thermal effects at elevated currents. Nevertheless, all deviations remain within ±5% of the measured value, which is consistent with the specified accuracy of the Hall probe in AC mode.

The magnetic field was not only measured at the center of the coils but also characterized along the x- and y-axes. Only three different frequencies were selected, as it had already been established that the frequency has almost no influence on the magnetic field, at least in terms of the magnetic flux density. Figure 8 shows the measured magnetic flux density (y-component of vector B) as a function of the x-position for three different frequencies, as well as a comparison with the simulation. Here, too, the experiment and simulation agree well, especially in the area where the magnetic field is homogeneous, that is, the central area between the two coils within R_i. For a correct measurement with the Hall probe, the field lines must be orthogonal to the probe. Since the field inside the Helmholtz coils is very homogeneous, the correct alignment of the probe also captures the correct magnitude of vector B. If the probe is not perfectly aligned (which is very difficult to achieve experimentally due to the limited space available for alignment), deviations may occur. However, this does not seem to be a significant problem given the excellent agreement between the measurement and simulation within R_i.

At 25 mm, the coil body begins; at 40 mm, the coil winding begins, and the measurement and simulation deviate somewhat more strongly from each other. Here, the field lines no longer run exactly parallel, so the correct magnitude of vector B can no longer be detected with a fixed alignment of the probe, resulting in a larger deviation between the experiment and simulation.

Figure 9 shows the magnetic flux density (y-component of vector B) along the y-axis for three different frequencies. Here, too, the experiment and simulation agree well, especially in the core region between the two coils ($y \leq 25$ mm). The magnetic field is symmetrical, so measurement in one direction is sufficient.

B. Fiber movement

In the following, the fiber dynamics are discussed separately for the transient response observed immediately after the magnetic field is switched on and for the steady-state response that develops after the system has reached a stable oscillation.

1. Steady-state response

First, the behavior of the fiber oscillation was examined in terms of its oscillation form and frequency for the steady-state response. Figure 10 shows a representative, randomly selected segment of the oscillation, illustrating the tracked fiber position relative to the median fiber position, which results in the deflection around the center point. For each frame, this deflection is calculated by the MATLAB script, resulting in a temporal resolution of 1 ms (at 1000 fps). The tracked fiber deflection (blue curve) corresponds very well with the sinusoidal fit (red dashed curve); the coefficient of determination R^2 is 0.9997.

The fit function used for Fig. 10 is

$$y = y_0 + A \cdot \sin\left(\frac{\pi \cdot (t - t_c)}{\frac{T}{2}}\right), \tag{3}$$

with the corresponding fit parameters in Table II.

10 August 2026 14:38:49

© Author(s) 2026

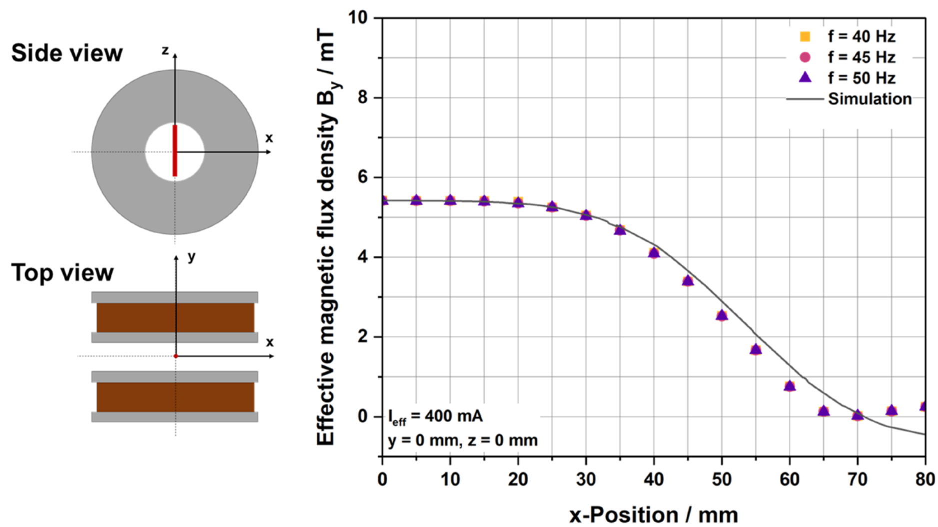

FIG. 8. Measured magnetic flux density (*y*-component of vector B) along the *x*-axis for two different frequencies and comparison with the simulation.

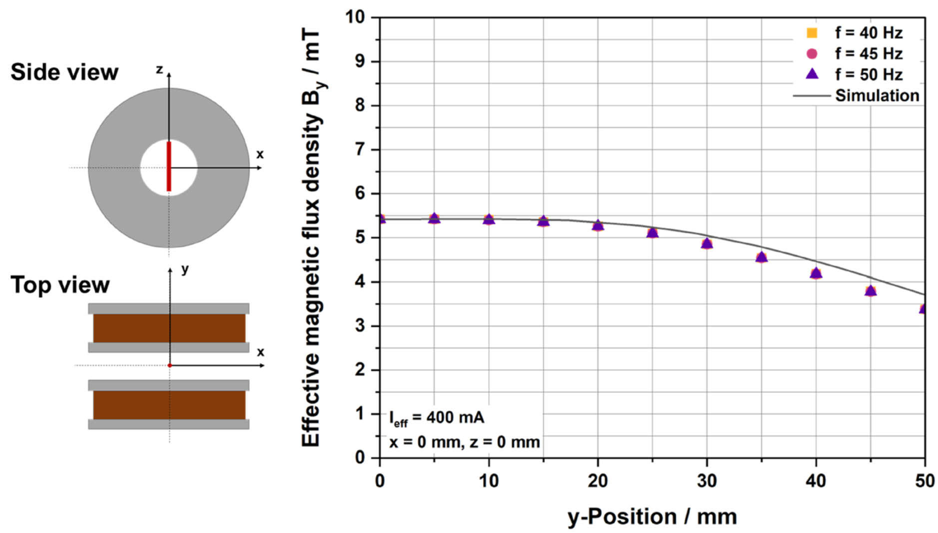

FIG. 9. Measured magnetic flux density (*y*-component of vector B) along the *y*-axis for different frequencies and comparison with the simulation.

10 August 2026 14:38:49

With the fitted period duration of 0.021 28 s, a frequency of 46.99 Hz results, which corresponds well with the driving frequency of f_d = 47 Hz.

The deflection and resulting acceleration of the fiber are shown in Fig. 11. The fiber deflection is shown on the left axis and the acceleration on the right axis. Even with very low magnetic flux densities of 0.77 mT (corresponding to a current of 58 mA), fiber deflections of 2.78 mm can be achieved, resulting in accelerations of 230 m/s^2 and more. Compared with Szabadi's[9] experiments using a constant magnetic field, the required power to reach the same maximum acceleration is reduced by a factor of 100. In comparison to static magnetic field excitation, the use of an alternating magnetic field yields comparable deflection amplitudes at significantly lower magnetic flux densities. This enhancement arises from the dynamic nature of the excitation: under sinusoidal driving, the magnetic torque periodically reverses direction, resulting in continuous acceleration and deceleration of the fiber within each cycle. In a static field, the magnetic torque acts only until mechanical equilibrium between magnetic and elastic restoring forces is reached, leading to a stationary deflected configuration without sustained acceleration. In contrast, alternating excitation continuously drives the system away from equilibrium. The periodic reversal of the magnetic field causes repeated acceleration toward alternating directions, thereby increasing the peak acceleration substantially compared to the static case.

As a consequence, dynamic magnetic excitation enables efficient generation of large oscillatory accelerations at comparatively low magnetic flux densities. This effect is particularly pronounced near resonance, where the interplay between periodic magnetic torque and the intrinsic dynamics of the fiber leads to amplified motion despite reduced field strength. However, from the second derivative of the stationary term of the deflection [second term in Eq. (6)] can be seen that the acceleration scales linearly with the deflection. Consequently, a reduction of the deflection to

© Author(s) 2026

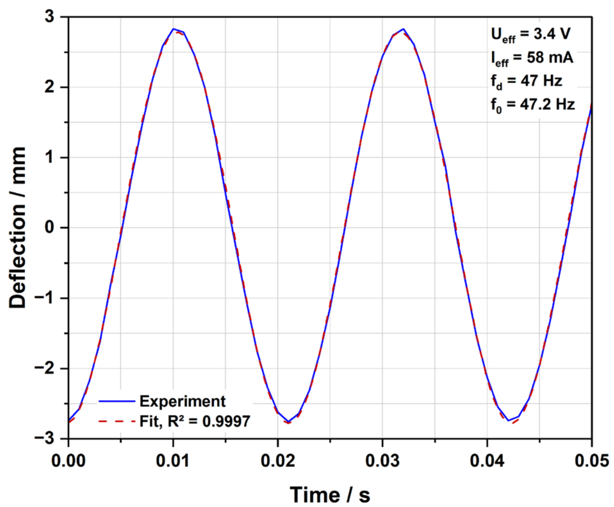

FIG. 10. Fiber deflection as a function of time for the steady-state response (blue line) and the sine fit (red, dashed line).

TABLE II. Fit parameters for the sine function in Fig. 10 and Eq. (3).

Parameter	Value	Meaning
y_0	0.0029 mm	Deflection offset
A	2.78 mm	Amplitude
t_c	0.0051 s	Time shift
T	0.021 28 s	Period

one-tenth results in a corresponding reduction of the acceleration to one-tenth.

To quantify the frequency response of the system, the driving frequency was varied in steps of 1 Hz while keeping the effective current constant (I_{eff} = 60 mA). For each frequency, the maximum steady-state amplitude was determined and plotted as a function of excitation frequency (see Fig. 12). The resulting curve exhibits a pronounced resonance peak in the vicinity of the natural frequency of the cantilevered fiber.

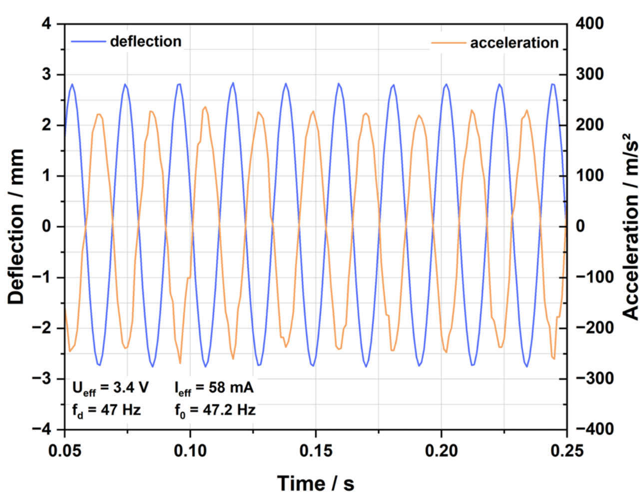

FIG. 11. Fiber deflection and second derivative (acceleration) as a function of time.

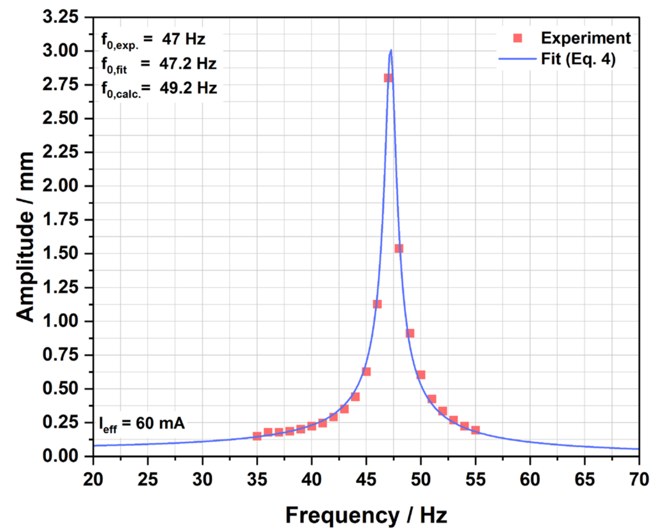

FIG. 12. Frequency dependence of the amplitude and fit with specified function [Eq. (4)].

The experimental data were fitted using the analytical amplitude expression of a driven damped harmonic oscillator [see Eq. (4)], where F_d represents the effective driving force amplitude, m is the effective mass of the oscillator, ω_0 is the natural angular frequency, ω_d is the driving angular frequency, and b is the viscous damping coefficient. The fit shows excellent agreement with the experimental data over the entire investigated frequency range. Treating F_d, b, and ω_0 as fitting parameters (see Table III) yields physically consistent values and confirms that the magnetically actuated fiber can be accurately described by the model of a driven damped harmonic oscillator in the investigated regime. Since the frequency was only varied in 1 Hz increments, the experimentally determined resonance frequency is $f_{0,exp.}$ = 47 Hz, the fit results in $f_{0,Fit}$ = 47.2 Hz, and the calculation according to Eq. (1) results in $f_{0,calc.}$ = 49.2 Hz:

$$A = \frac{F_d}{\sqrt{m^2\left(\omega_0^2 - \omega_d^2\right)^2 + b^2\omega_d^2}}, \quad (4)$$

where F_d is the amplitude of the driving force, m is the mass of the oscillator, $m = 2.074 \cdot 10^{-6}$ kg, ω_0 is the natural angular frequency, ω_d is the driving angular frequency, and b is the damping coefficient.

TABLE III. Fit parameters for the fit function in Fig. 12 and Eq. (4).

Parameter	Value	Meaning
F_d	$1.166 \cdot 10^{-5}$ N	Amplitude of driving force
ω_0	296.67 rad/s	Natural angular frequency
b	$1.298 \cdot 10^{-5}$ kg/s	Damping coefficient

10 August 2026 14:38:49

© Author(s) 2026

The value of the fitted natural angular frequency gives a value of 47.2 Hz for the natural frequency f_0. The value of the driving force is only 57% of the weight force of the fiber. However, the driving force does not have to work against gravity, but against the bending stiffness of the fiber.

Although the magnetic interaction physically produces a distributed aligning torque[10] along the fiber [see Eq. (5)], rather than a concentrated force, the system was modeled using an equivalent point force F_d acting at the fiber tip. This simplification allows the response to be described by the standard amplitude expression of a driven damped harmonic oscillator and was found to reproduce the experimental frequency response with sufficient accuracy:

$$T = M \times B \times V \times \sin \Theta, \tag{5}$$

where T is the torque, M is the magnetization, V is the volume of the fiber, and Θ is the angle between M and B.

This does not imply that a point force acts on the fiber. Instead, the magnetic field induces a distributed magnetic torque along the fiber, which results in a bending moment and, consequently, transverse deflection of the fiber. Within the framework of modal analysis, the distributed torque then appears as an equivalent generalized force driving this mode. The fitted parameter F_d therefore represents an effective modal driving force that captures the net dynamic effect of the spatially distributed magnetic torque. This reduction to an equivalent force-driven oscillator is justified in the investigated regime, as the response is dominated by the first bending mode and higher-order modes are not significantly excited.

In addition to the frequency sweep, the dependence of the steady-state amplitude on the effective current was investigated at three selected driving frequencies (see Fig. 13). For all examined frequencies, the amplitude increases linearly with increasing current.

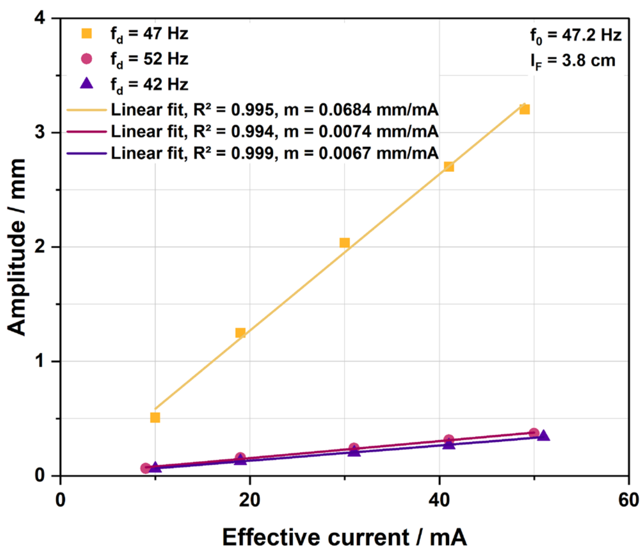

FIG. 13. Influence of current on the amplitude of fiber oscillation at three different driving frequencies (symbols) and respective linear fit (lines).

This behavior is consistent with the underlying actuation mechanism: the magnetic torque is proportional to the magnetic flux density [compare Eq. (5)], which in turn scales linearly with the coil current [compare Eq. (2)]. Consequently, the effective driving force amplitude F_d is proportional to the current, and the oscillator model predicts a linear scaling of the response amplitude for a fixed excitation frequency.

The slope of the amplitude–current characteristic depends strongly on the proximity to resonance. When the driving frequency is close to the natural frequency, the denominator in the harmonic oscillator response function becomes small [compare Eq. (4)], leading to enhanced sensitivity of the amplitude to variations in driving force. Accordingly, the largest slope is observed near resonance, whereas significantly smaller slopes are obtained for excitation frequencies further away from the resonance frequency. If the selected frequencies are equally spaced from the resonance frequency, the measured slope of the deflection as a function of the current is the same.

2. Transient response

When the high-speed camera is triggered synchronously with the activation of the AC source, the transient response of the fiber is recorded immediately after the onset of magnetic excitation. The transient behavior depends strongly on the selected driving frequency. Representative time traces for driving frequencies between 43 and 53 Hz are shown in Fig. 14. As expected, the maximum amplitude varies significantly with excitation frequency, reflecting the proximity to resonance. The observed transient oscillation can be interpreted within the framework of the driven damped harmonic oscillator. The general solution of the equation of motion consists of two contributions: the homogeneous solution, describing free oscillation at the natural frequency with exponentially decaying amplitude due to damping [first term in Eq. (6)], and the particular solution, corresponding to the steady-state response at the driving frequency [second term in Eq. (6)]:

$$x(t) = A_0 e^{-\frac{b}{2m}t} \cos(\omega_0 t + \delta) + A \cos(\omega_d t - \delta), \tag{6}$$

where x(t) is the position of the fiber at time t, A_0 is the amplitude due to resonance excitation, b is the damping coefficient, m is the mass of the fiber, ω_0 is the natural angular frequency, ω_d is the driving angular frequency, and δ is the phase constant.

Immediately after excitation, both components are present simultaneously. Their superposition leads to a modulation of the oscillation amplitude whenever $f_d \neq f_0$.

This amplitude modulation corresponds to a beat phenomenon that arises from the interference of two closely spaced frequencies, namely, the natural frequency and the driving frequency. Fast Fourier transform (FFT) analysis clearly resolves both components during the transient phase. The beat frequency is given by the absolute difference $|f_d - f_0|$, which determines the envelope period of the transient oscillation. As the driving frequency approaches resonance, the frequency difference decreases, leading to slower beat modulation. At exact resonance, the homogeneous and particular

10 August 2026 14:38:49

© Author(s) 2026

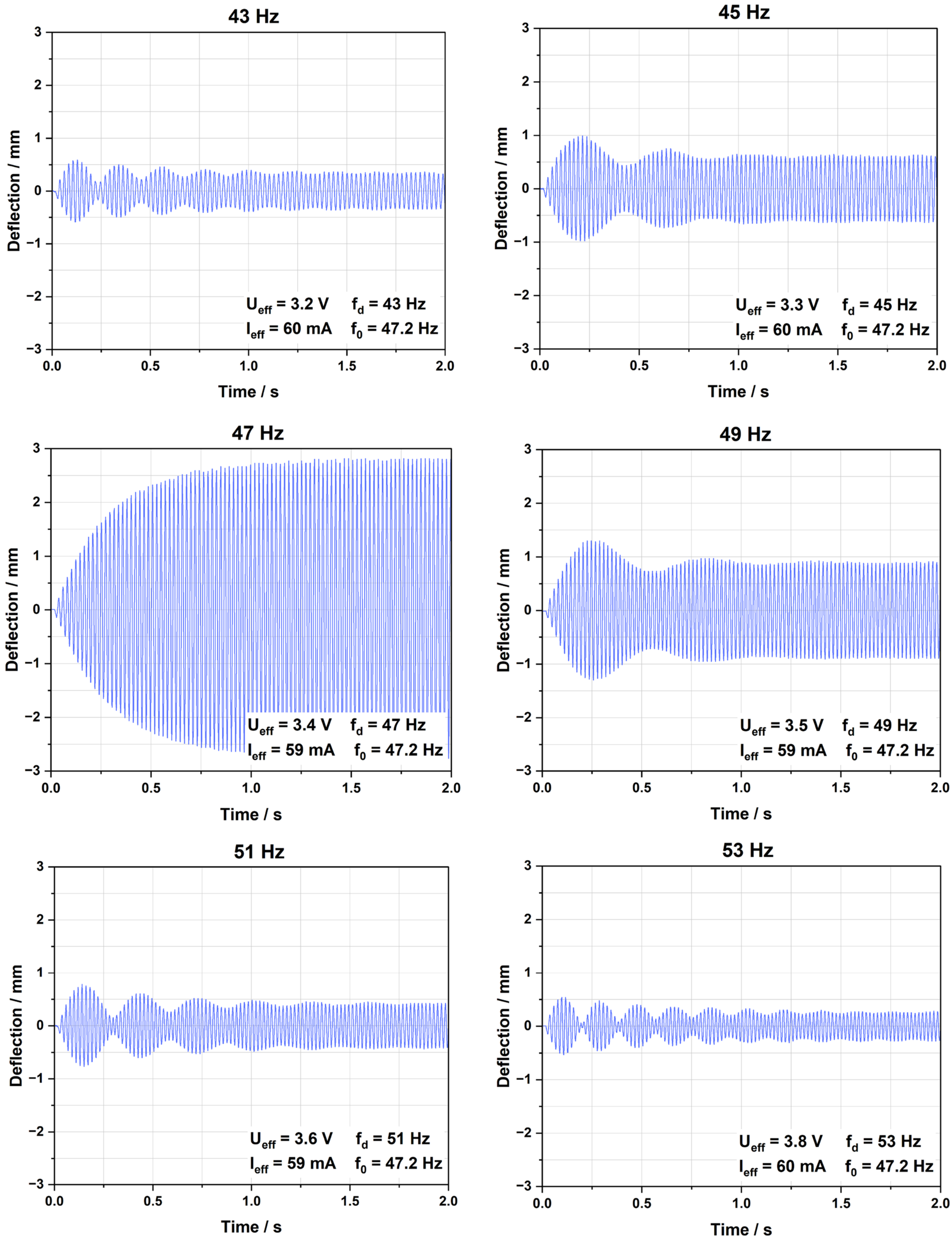

FIG. 14. Overview of different transient responses of the fiber depending on its driving frequency.

10 August 2026 14:38:49

© Author(s) 2026

solutions oscillate at the same frequency, and no beat pattern is observed; instead, the response evolves monotonically toward the steady-state amplitude.

IV. CONCLUSION

The present study systematically investigated the dynamic behavior of a magnetizable cantilevered single fiber subjected to a spatially homogeneous alternating magnetic field generated by a Helmholtz coil arrangement. The magnetic field was characterized experimentally using Hall probe measurements and numerically by finite element simulations in COMSOL Multiphysics. The excellent agreement between measurement, analytical calculation, and simulation confirms that the magnetic field within the Helmholtz configuration can be described with high accuracy over the investigated frequency and current ranges.

The fiber dynamics were analyzed by high-speed imaging combined with automated MATLAB-based motion evaluation, enabling the quantitative determination of deflection, velocity, and acceleration. Under steady-state conditions, the fiber exhibits purely harmonic oscillation at the driving frequency. The experimentally determined frequency response shows a pronounced resonance peak near the theoretically predicted natural frequency of the cantilevered beam. The measured resonance frequency agrees well with both the analytical Euler–Bernoulli beam model and the fitted harmonic oscillator model, confirming that the first bending mode dominates the response.

The frequency-dependent amplitude behavior is accurately described by the analytical solution of a driven, damped harmonic oscillator. Although the magnetic interaction physically manifests as a distributed aligning torque, the dynamic response can be reduced to an equivalent modal driving force acting on the dominant bending mode. This modal reduction provides a consistent and physically justified interpretation of the fitted parameters, including the effective driving force and damping coefficient.

The transient response reveals the superposition of the natural and driving frequencies immediately after field activation. For off-resonant excitation, this leads to a characteristic beat phenomenon whose envelope frequency corresponds to the difference between the natural and driving frequencies. As the homogeneous solution decays due to damping, the motion converges to the steady-state response governed solely by the driving frequency. The experimental observations are in full agreement with the theoretical solution of the linear, damped oscillator.

A key finding of this study is that alternating magnetic excitation enables the generation of large oscillatory accelerations at comparatively low magnetic flux densities. In contrast to static magnetic deflection, the periodic reversal of the magnetic field continuously drives the system away from equilibrium, resulting in significantly enhanced peak accelerations, particularly near resonance. This dynamic amplification effect allows a substantial reduction in the required magnetic field strength, and thus energy input, compared to static actuation for similar maximum acceleration values.

Overall, the combination of precise magnetic field characterization, high-resolution motion analysis, and analytical modeling establishes a comprehensive framework for describing magnetically induced oscillations of slender magnetizable structures. The validated physical understanding provides a solid basis for future investigations involving the oscillation of particle-laden fibers, where magnetically induced accelerations, and thus inertial forces acting on particle deposits, may be employed as a contactless and energy-efficient strategy for particle detachment in situations where conventional cleaning methods are not feasible.

ACKNOWLEDGMENTS

This work was supported by the Deutsche Forschungsgemeinschaft (DFG, German Research Foundation)—Grant No. 529328968.

The authors gratefully acknowledge Dr. Guthausen for providing the Hall probe used in this study.

AUTHOR DECLARATIONS

Conflict of Interest

The authors have no conflicts to disclose.

Author Contributions

Nadine May: Data curation (lead); Formal analysis (lead); Investigation (lead); Methodology (lead); Project administration (lead); Software (lead); Validation (lead); Visualization (lead); Writing – original draft (lead); Writing – review & editing (equal). **Jörg Meyer**: Conceptualization (equal); Funding acquisition (equal); Project administration (supporting); Supervision (equal); Writing – review & editing (equal). **Matthias Franzreb**: Methodology (supporting); Supervision (supporting); Writing – review & editing (equal). **Achim Dittler**: Conceptualization (lead); Funding acquisition (equal); Project administration (supporting); Resources (lead); Supervision (equal); Writing – review & editing (equal).

DATA AVAILABILITY

The data that support the findings of this study are available from the corresponding author upon reasonable request.

REFERENCES

[1] P. Bächler, J. Meyer, and A. Dittler, "Operating behavior of pulse jet-cleaned filters regarding energy demand and particle emissions—Part 1: Experimental parameter study," Chem. Eng. Technol. **46**(8), 1689–1697 (2023).

[2] F. Gerbal, Y. Wang, F. Lyonnet, J.-C. Bacri, T. Hocquet, and M. Devaud, "A refined theory of magnetoelastic buckling matches experiments with ferromagnetic and superparamagnetic rods," Proc. Natl. Acad. Sci. U. S. A. **112**(23), 7135–7140 (2015).

[3] H. A. Wheeler, "Simple inductance formulas for radio coils," Proc. IRE **16**(10), 1398–1400 (1928).

[4] T. H. Fawzi and P. E. Burke, "The accurate computation of self and mutual inductances of circular coils," IEEE Trans. Power Appar. Syst. **97**(2), 464–468 (1978).

[5] D. Gross, W. Hauger, J. Schröder, and W. A. Wall, *Technische Mechanik 2: Elastostatik* (Springer, Berlin, Heidelberg, 2024).

10 August 2026 14:38:49

© Author(s) 2026

[6]The MathWorks, Inc., MATLAB version: 24.2.0 (R2024b), 2024.
[7]A. Savitzky and M. J. E. Golay, "Smoothing and differentiation of data by simplified least squares procedures," Anal. Chem. **36**(8), 1627–1639 (1964).
[8]M. S. Crosser, S. Scott, A. Clark, and P. M. Wilt, "On the magnetic field near the center of Helmholtz coils," Rev. Sci. Instrum. **81**(8), 084701 (2010).
[9]J. Szabadi, J. Meyer, and A. Dittler, "Particulate matter detachment from a magnetizable single fiber applying magnetic forces in ambient air," Separations **10**(5), 297 (2023).
[10]M. Weber, R. Koch, and K. H. Rieder, "UHV cantilever beam technique for quantitative measurements of magnetization, magnetostriction, and intrinsic stress of ultrathin magnetic films," Phys. Rev. Lett. **73**(8), 1166–1169 (1994).

10 August 2026 14:38:49

© Author(s) 2026